Plasma Phys. Control. Fusion **51** (2009) 055017 (17pp) doi:10.1088/0741-3335/51/5/055017

On visibility of carbon dust particles in fusion plasmas with fast framing cameras

R D Smirnov[1], S I Krasheninnikov[1], J H Yu[2], A Yu Pigarov[1], M Rosenberg[3] and J L Terry[4]

[1] Department of Mechanical and Aerospace Engineering, University of California San Diego, La Jolla, CA 92093, USA
[2] Center for Energy Research, University of California San Diego, La Jolla, CA 92093, USA
[3] Department of Electrical and Computer Engineering, University of California San Diego, La Jolla, CA 92093, USA
[4] MIT Plasma Science and Fusion Center, Cambridge, MA 02139, USA

E-mail: rsmirnov@ucsd.edu

Received 6 November 2008, in final form 20 February 2009
Published 9 April 2009
Online at stacks.iop.org/PPCF/51/055017

Abstract
The visibility of carbon dust particles in fusion plasmas with fast framing cameras is evaluated using computer and theoretical modelling. Dust heating and ablation in the plasmas, ionization dynamics of the ablation cloud around the dust particle, thermal radiation of the dust and line radiation of the cloud are considered. The minimal size of carbon dust particles visible with the cameras is calculated as a function of the plasma parameters and the distance from the dust to the camera objective. The relative contributions of thermal radiation from the grain and line radiation from the cloud to the total dust radiation are analysed.

1. Introduction

The production and accumulation of dust in high load fusion devices, such as ITER, can lead to numerous safety and operational issues. These include high chemical reactivity of dust, tritium retention and transport by dust, plasma contamination with dust material, discharge termination by large particles, damage of the first wall and diagnostic instruments by high speed dust particles, etc [1–6]. In order to study and effectively control dust behaviour in fusion plasmas, *in situ* dust diagnostic techniques are required. Extensive experimental data are also needed for development and validation of available theoretical models and computational codes for modelling of dust dynamics in fusion plasmas, such as DUSTT and DTOKS codes [7–9], to provide reliable predictive results for ITER. In recent years various experimental tools of dust surveying and analysis have been developing, among which are the observation and tracking of dust particles by fast framing cameras, dust size measurements by laser light scattering, measurements of the amount of accumulated dust on inner vessel surfaces with electrostatic and gravimetric detectors [10–18]. The only method allowing at present the real

time tracking of dust particles in fusion plasmas is the imaging with fast framing cameras. The imaging of small dust grains in fusion plasmas is possible because heating and ablation of the grains by impinging plasma particles creates two sources of radiation: (i) thermal radiation from the heated dust and (ii) line and continuum radiation from the ablation cloud surrounding the particle due to various interaction processes of the ablated material with the plasma (e.g. excitation, recombination, Bremsstrahlung radiation, etc). The observation and tracking of dust with cameras are currently performed on practically all major fusion machines. The obtained results provide firm confirmation of the presence of dust in fusion plasmas, dependences of the number of visible dust particles on device operation mode and observation location, and data on dust dynamics including dust trajectories and speeds [6, 10, 13, 19–22]. However, it is not clear how the camera imaging characterizes the dust particles themselves. The analysis of dust images brings up questions about what dust is visible—what is the size, temperature, composition of visible grains? What radiation is detected—is it thermal radiation from the particle or line radiation from the ablation cloud? Where is dust visible—under which surrounding plasma conditions? In this paper we attempt to answer these questions in a first approximation using analytical and numerical modelling of dust heating/ablation in plasmas, ionization dynamics of the ablation cloud and intensity of the radiation from both the particle and the ablation cloud, which is then convolved with spectral sensitivity of a test camera system to draw preliminary conclusions on dust visibility in the plasmas. In this paper we consider dust particles that are small enough so that we can neglect shielding of dust grains by the ablated dust material, and assume that the ablation cloud does not substantially change the local plasma parameters. The physics of dust heating/ablation in this situation is significantly different from that of bigger pellets, for which the shielding effects of the ablation cloud are of crucial importance, as e.g. in the Parks ablation model [23]. We estimate that these approximations hold for particles with radius smaller than several tens of micrometres [24].

The paper is organized as follows: section 2 describes the test camera system; the dust heating and ablation model is presented in section 3; calculations of thermal radiation from dust grains for various plasma conditions are given in section 4; section 5 describes the analytical model and solutions for ionization dynamics of the ablation cloud around the dust particle; the line radiation from the carbon atoms and ions in the ablation cloud is calculated in section 6; the total radiation of the dust particle and its visibility with the cameras is analysed in section 7. The results are summarized and conclusions are presented in section 8.

2. Camera system on DIII-D

In order to analyse dust visibility in fusion plasmas in this paper we use, as an example, the measured spectral sensitivity and optical characteristics of a fast framing camera system employed on the DIII-D tokamak. Although experimental camera systems on other tokamaks may differ somewhat from that on DIII-D, they are generally alike in basic schematics and use similar components. Hence, we assume that the dust visibility analysis provided in this paper is applicable as a ball park approximation to many similar camera systems on other fusion devices. In addition, the analysis method presented here can be applied to camera systems with different spectral sensitivities in a straightforward manner.

Here we point out major properties of the optical system used for dust observations on DIII-D. The reader can also find additional details in [19, 25]. The sketch of the system is shown in figure 1. The objective lens collects light from an observed luminous object in the plasma and focuses it on the front face edge of a coherent fibre bundle composed of 800×1000 individual fibres, each one of diameter $D_{\text{fib}} = 8\,\mu\text{m}$. The bundle's front edge is aligned with the focal plane of the objective. The focal length of the objective is $f = 12\,\text{mm}$, so that

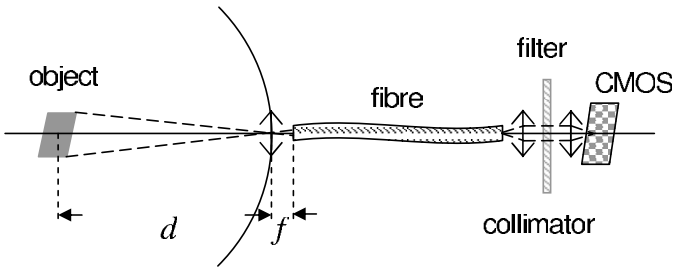

Figure 1. The sketch of the optical system used for dust observations on DIII-D.

objects at distance d from the objective lens of order of a metre or larger produce a sharp real image at the bundle's edge. The coherent fibre bundle transfers the image, preserving its size and layout, to the opposite face edge, to a location where the fast framing camera and other components can be conveniently and safely placed. Light exiting the fibre bundle is collimated and refocused onto the camera CMOS detector. The collimator serves the purpose of applying filters to the system for measurements of its spectral sensitivity, and together with the camera's optics forms an image on the sensor preserving the same linear sizes of the image as at the face edge of the fibre bundle. Therefore, the linear magnification factor of the whole optical system is $\beta = f/d$. Note that in general the focal lengths of the collimator's lenses can be different. In such a case, the magnification factor β should be multiplied by the ratio of the focal length of the focusing lens to the focal length of the collimating lens.

The optical system on DIII-D utilizes a Phantom v7.1 fast framing camera, which has a CMOS sensor with typical resolution 256 × 256 pixels, 12bit (4096 counts) per pixel data channel, linear pixel size $L_{\rm px} = 22\,\mu$m and the available range of frame rates is 10^2–3×10^4 frames s^{-1}. The spectral response of the whole optical system was measured during a scheduled maintenance period between DIII-D experimental campaigns in summer 2007. The measurements employed a calibrated light-integrating sphere as an *in situ* light source and a set of interference filters for a number of lines within the camera's spectral sensitivity range, which are commonly utilized in various diagnostics (D_α, C II, C III, Ar I, etc). The spectral response of the system, $P(\lambda)$, is shown in figure 2, where the measurement points are indicated as black squares. The spectral sensitivity of the sensor and the transmission of the fibre bundle are the two major contributors in the system's spectral response curve. The fibre bundle and the lenses significantly limit the system's response in UV and the short wavelength end of visible spectrum up to ∼500 nm. At the longer wavelength end the spectral transmission of the bundle and the camera optics is approximately flat. In the long wavelength visible and near IR regions, the sensor's sensitivity is the main limiting factor in the spectral response of the system. The response was measured in the range of wavelengths 434–696 nm with one additional measurement point in the near IR, which was used as a reference point for extrapolation of the sensitivity curve up to 1000 nm employing data on the sensor's quantum efficiency provided by the manufacturer of the camera [26]. Thus, the effective spectral response of the system shown in figure 2 covers the range of wavelengths 434–1000 nm and peaks around ∼650 nm. We assume that radiation outside of the indicated range of the wavelengths is not detected by the camera.

The relative error with which the effective spectral response of the system was determined is estimated as ∼10%, which is sufficiently small for the purposes of evaluation of dust visibility by the camera. We also note that during experimental campaigns on DIII-D the transmission of the fibre bundle is continuously degraded due to neutron irradiation

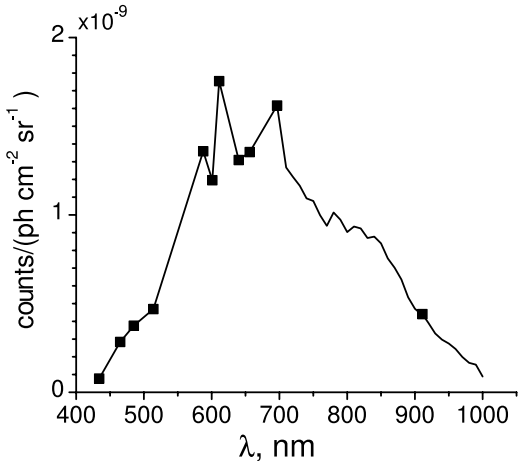

Figure 2. The effective spectral response of the camera system on DIII-D. The black squares represent the experimentally measured data points.

produced by the plasma discharges. The neutron exposure leads to gradual deterioration of the bundle's transmission in UV and short wavelength visible regions of the spectrum, but does not significantly affect the transmission at longer wavelengths, which was verified with measurements of the bundle's spectral transmission after the experimental campaign. Thus, this effect may have only a marginal impact on the following calculations, as most of dust's thermal and line radiation considered in this paper covers the near IR and long wavelength visible spectrum.

3. Dust heating and ablation

In this paper we consider a spherical carbon dust particle of radius R_d placed in a fully ionized deuterium plasmas with plasma density n_e and temperature $T_e = T_i$, which are treated as independent parameters. The ion and electron flows to the dust particle lead to its continuous heating and ablation. Besides the heat transfer from the plasma, the carbon dust also almost completely absorbs energy released due to ion recombination on its surface. At the same time, the dust cooling occurs due to thermal radiation, ablation and electron emission. Assuming that the dust particle survives for sufficient duration in the plasma, dust heating and cooling become balanced at a certain temperature of the particle. To find this temperature and the dust ablation rate corresponding to it we used the dust heating and ablation model from the DUSTT code described in detail in [7, 8]. The model takes into account the heating and cooling mechanisms mentioned above as well as ablation of the carbon dust particle due to thermal and radiation enhanced sublimation, physical and chemical sputtering. The flux of thermally sublimated atoms from the dust at a temperature T_d is calculated as maximal sublimation flux in vacuum [27, 28] $\Gamma_{sub} = P/\sqrt{2\pi M_C k_B T_d}$, where k_B is Boltzmann's constant, M_C is the mass of a carbon atom and P is the saturated vapour pressure of carbon atoms. Because carbon at high temperatures sublimates mostly in the form of clusters, we calculate the effective flux of the sublimated carbon atoms and the corresponding cooling power based on the saturated vapour pressure and the enthalpy of formation of the clusters found in JANAF tables [29]. The resulting effective saturated vapour pressure of carbon atoms as a function of dust temperature is fitted by expression $P = 10^{B-A/T_d}$, where P is in Pa, T_d is in K, $B = 14.522$, and

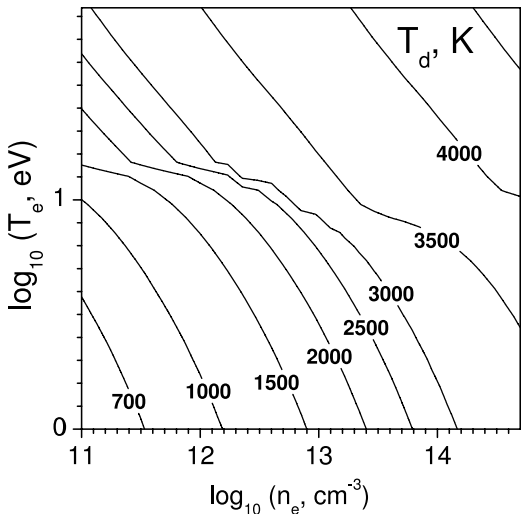

Figure 3. The calculated temperature of the carbon dust particle in a deuterium plasma as a function of the plasma parameters.

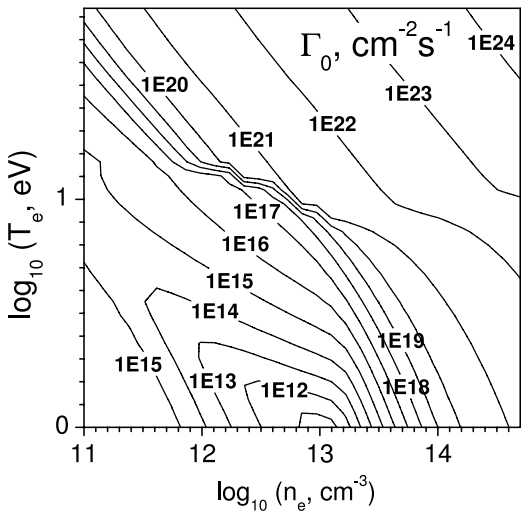

Figure 4. Total effective flux Γ_0 of ablated atoms from carbon dust in a deuterium plasma as a function of plasma parameters.

$A = 38286$. The calculated temperature of dust as a function of the plasma parameters is shown in figure 3. As can be seen, the particle reaches temperature of a few 1000 K in tokamak plasmas, which allows it to radiate effectively in the visible and near IR range. In figure 4 the calculated total effective flux of ablated atoms from the dust, Γ_0, which includes sublimated and sputtered atoms is plotted as a function of the plasma parameters, n_e and T_e. Comparing figures 3 and 4 one can see that significant dust ablation occurs in plasmas where the dust temperature exceeds ∼3000 K. In such plasmas we can expect noticeable thermal radiation from the dust particle and the formation of an appreciable ablation cloud around it.

4. Thermal radiation

The thermal radiation of the dust particle under different plasma conditions can be calculated knowing the dust temperature obtained in the previous section. The spectral radiant emittance of a black body with temperature T_d according to Planck's law is

$$I_\mathrm{P}(\lambda, T_\mathrm{d}) = \frac{2\pi hc^2}{\lambda^5} \frac{1}{\exp(hc/\lambda k_\mathrm{B} T_\mathrm{d}) - 1}, \tag{1}$$

where h is Planck's constant, c is the speed of light and λ is the radiation wavelength. In order to calculate thermal radiation from a dust particle we need to know its spectral emissivity. In general, the spectral emissivity of a small particle is a function of the temperature dependent optical properties of the particle's material and its size to wavelength ratio [30, 31]. The spectral emissivity of a spherical dust particle can be calculated using Mie theory [32], once the complex index of refraction of the dust material is available. However, the optical properties of dust in fusion devices as well as their dependence on temperature are unknown. In this paper we neglect these dependences and assume a constant value of the carbon dust emissivity $\varepsilon = 0.8$. This number is close to the total emissivity of amorphous graphite, which is weakly dependent on temperature. The same value of the emissivity was used in the calculations of radiative dust cooling in section 3. We also neglect the dependence of the emissivity on dust size in order to simplify further calculations. According to Mie theory, such approximation can be justified for particles with radius larger than $\sim \lambda_\mathrm{m}/2\pi|n|$, where $\lambda_\mathrm{m} \sim 1\,\mu$m is a characteristic wavelength of the thermal radiation and $|n|$ is the absolute value of the complex index of refraction of dust material. This limits our consideration to particles with $R_\mathrm{d} > 0.1\,\mu$m. As we will see further in this paper, this limit is below a minimal size of dust visible by the camera in typical SOL plasmas.

Equation (1) multiplied by the particle's emissivity ε and then convolved with the spectral response of the camera system $P(\lambda)$ gives the camera signal due to thermal radiation from dust, S_th, in counts per unit time from a pixel where the dust image is formed:

$$S_\mathrm{th} = \frac{\varepsilon}{hc\mu} \int I_\mathrm{P}(\lambda, T_\mathrm{d})\, P(\lambda)\, \lambda\, \mathrm{d}\lambda, \qquad \mu \equiv \left(\frac{L_\mathrm{px}}{\beta R_\mathrm{d}}\right)^2. \tag{2}$$

Here we assume that the grain radiates isotropically in the total solid angle, 4π sr. The factor μ^{-1}, which is proportional to the ratio of the dust particle's surface area to the view-line projected pixel area at distance d, appears because the camera's spectral response function, $P(\lambda)$, is obtained for a light source illuminating a whole pixel, while here we consider the dust thermal image that is smaller than the pixel area on the camera detector. Due to the very small dust size and typically small magnification factor β, the size of dust image on the sensor is usually limited by diffraction or the size of individual fibres in the bundle. So, in order to satisfy our assumption the pixel size L_px should be larger than the individual fibre's diameter, D_fib, and the diameter of the Airy disc of the dust image, $D_\mathrm{A} = 2.44\lambda_\mathrm{m}/\mathcal{N}A$, where $\mathcal{N}A$ is the numerical aperture of the optical system. For the considered camera system with $L_\mathrm{px} = 22\,\mu$m, $D_\mathrm{fib} = 8\,\mu$m, $\mathcal{N}A \sim 0.4$ and $\lambda_\mathrm{m} \sim 1\,\mu$m, this requirement is satisfied. In the case when the dust thermal image covers multiple pixels, the total projected area and the combined signal of an illuminated group of pixels can be considered. The important consequence following from equation (2) is that the camera signal induced by the thermal radiation of the dust particle is proportional to the particle's radius squared and is inversely proportional to square of the distance from the particle to the objective.

The number of thermal signal counts recorded with a camera in one frame can be obtained multiplying the signal S_th by the frame exposure time. Here we assume that dust radius does not change significantly during the frame exposure. However, this might not be the case for

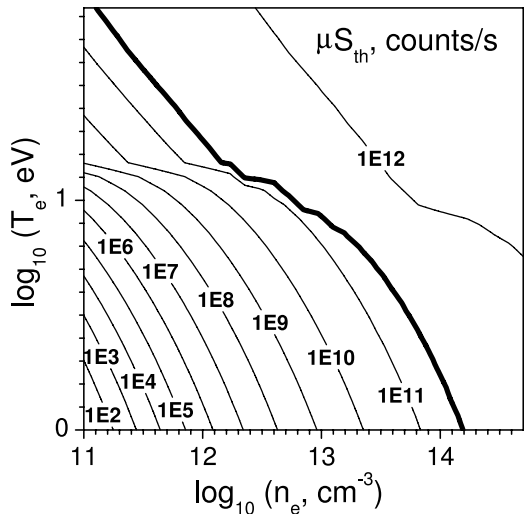

Figure 5. The calculated camera signal induced by the dust's thermal radiation as a function of plasma parameters. Above the thick black curve a carbon dust particle of radius $R_d = 1\,\mu$m is visible by the camera from distance $d = 1$ m assuming 1 ms frame exposure time and 100 counts sensitivity threshold.

small particles in hot plasmas near the separatrix. Also some dust particles may have very high speed $\sim$1 km s^{-1} [19, 21, 33] and cross the projected pixel region in shorter time than the exposure time. For such dust particles, which are substantially destroyed or move out of the projected pixel region during the frame exposure time, the actual number of signal counts recorded in the pixel would be smaller than the one obtained using this time, so the particles may become undetectable. In a first approximation this effect can be taken into account by introducing an effective exposure time, which would be of order of the characteristic time of dust destruction or the time of dust transit through the projected pixel region, whichever is shorter. In a more rigorous approach the coupled dynamics of dust motion and ablation can be considered and a time integrated camera signal can be calculated. In this paper, however, we aim to find basic relations between the dust characteristics and the radiation and leave further complications for future consideration.

In figure 5 the camera's thermal radiation signal S_{th} multiplied by the factor μ is plotted as a function of the parameters of the plasma, where the dust resides. In the area of the plot above the thick black curve a carbon dust particle of radius $R_d = 1\,\mu$m is visible with the camera from distance $d = 1$ m, assuming 1 ms frame exposure time and a sensitivity threshold of 2.4% of the full dynamic range (100 counts for a 12 bit detector). This curve and the corresponding values of the exposure time and the camera's threshold sensitivity are given as an example and may be different for different experimental conditions. The threshold may depend on the sensor's noise level, as well as on the background plasma radiation. The indicated threshold value of 100 counts roughly corresponds to the experimentally measured level of the background camera signal on DIII-D [25]. As can be seen in figure 5, the thermal radiation of a micrometre dust particle just becomes visible under typical SOL plasma conditions ($n_e = 10^{13}$ cm^{-3}, $T_e = 10$ eV) with the camera. Increasing or decreasing the dust size by one order of magnitude would shift the visibility boundary by two orders of the value of the signal. As figure 5 shows, the variation of the dust's thermal radiation signal is strong at the lower plasma densities and temperatures and weak at the higher ones, which makes even big

particles hard to see in cold and tenuous plasmas. Note that the dust dwell time in hot and dense plasmas can be smaller than the assumed exposure time of 1 ms; in such cases the actual dust visibility threshold would shift towards larger signal values per unit time.

5. Ionization dynamics of ablation cloud

As described in section 3, sublimation and sputtering of dust material by the plasma lead to the formation of an ablation cloud around the dust particle. The ablated material expands into the plasma and becomes excited and multiply ionized due to collisions with the plasma electrons. In order to analyse radiation from the cloud, we need to consider the spatial distributions of carbon species of different ionization states in the cloud and the radiation from them. Given the purposes of this paper, i.e. to provide estimates on the dust visibility by the fast framing cameras, and available atomic data for the carbon species we develop a simple 1D model of the ablation cloud dynamics taking into account only the major processes contributing to the cloud's composition and radiation. In this model we assume that atoms of the ablated dust material advance into the plasma with a constant speed $u_0 = \sqrt{k_B T_d/(2\pi M_C)}$ that equals the average unidirectional Maxwellian speed defined by the dust temperature. We estimate the rate of carbon–deuterium momentum transfer collisions as $\sim 10^{-9}$–10^{-10} cm^3 s^{-1} according to the collision cross section from [34] for the plasma temperatures in the range from 1 to 100 eV. This gives us the momentum transfer mean free path of order of a few centimetres for a carbon particle with speed $\sim 10^5$ cm s^{-1} (corresponding to the dust sublimation at temperatures of a few thousand kelvin) in the plasmas with densities $\sim 10^{13}$–10^{14} cm^{-3}. The estimated mean free path is somewhat larger than the size of part of the ablation cloud within the projected pixel region which is less than 1 cm. Thus, the assumption of a constant speed of the ablated carbon particles can be approximately satisfied in the considered part of the cloud.

The flow of ablated carbon atoms is ionized by the surrounding plasma electrons going through subsequent ionization states C I, C II, C III, etc. Neglecting ion recombination, which will be discussed later in this section, and assuming that the electron density and temperature is uniform we can write a set of 1D continuity equations for the cloud components in Lagrangian form:

$$\begin{cases} \mathrm{d}I_{\mathrm{C\,I}}/\mathrm{d}t = -K^{\mathrm{C\,I}} n_e I_{\mathrm{C\,I}}, \\ \mathrm{d}I_{\mathrm{C}j}/\mathrm{d}t = -K^{\mathrm{C}j} n_e I_{\mathrm{C}j} + K^{\mathrm{C}j-1} n_e I_{\mathrm{C}j-1}, \qquad \mathrm{C}j > \mathrm{C\,I}, \\ I_{\mathrm{C\,I}}(t=0) = I_0 = 4\pi R_d^2 \Gamma_0, \\ I_{\mathrm{C}j}(t=0) = 0, \qquad \mathrm{C}j > \mathrm{C\,I}, \end{cases} \tag{3}$$

where $I_{\mathrm{C}j}(t)$ is the particle current and $K^{\mathrm{C}j}$ is the ionization rate of jth carbon component, correspondingly. The initial flux of carbon atoms at the dust surface Γ_0 was calculated in section 3 and is given in figure 4. Because the speed of ablated particles, u_0, is constant in this model, the distance from a carbon particle in the cloud to the dust surface is $z = u_0 t$. The analytical solution of equation (3) is obtained as

$$\begin{cases} I_{\mathrm{C\,I}}(t) = I_0 \exp\left(-K^{\mathrm{C\,I}} n_e t\right) \\ I_{\mathrm{C\,II}}(t) = I_0 K^{\mathrm{C\,I}} \left[-\exp\left(-K^{\mathrm{C\,I}} n_e t\right) + \exp\left(-K^{\mathrm{C\,II}} n_e t\right)\right] / \left(K^{\mathrm{C\,I}} - K^{\mathrm{C\,II}}\right) \\ I_{\mathrm{C\,III}}(t) = I_0 K^{\mathrm{C\,I}} K^{\mathrm{C\,II}} \begin{bmatrix} \exp\left(-K^{\mathrm{C\,I}} n_e t\right) / \left[\left(K^{\mathrm{C\,I}} - K^{\mathrm{C\,II}}\right)\left(K^{\mathrm{C\,I}} - K^{\mathrm{C\,III}}\right)\right] \\ -\exp\left(-K^{\mathrm{C\,II}} n_e t\right) / \left[\left(K^{\mathrm{C\,I}} - K^{\mathrm{C\,II}}\right)\left(K^{\mathrm{C\,II}} - K^{\mathrm{C\,III}}\right)\right] \\ +\exp\left(-K^{\mathrm{C\,III}} n_e t\right) / \left[\left(K^{\mathrm{C\,I}} - K^{\mathrm{C\,III}}\right)\left(K^{\mathrm{C\,II}} - K^{\mathrm{C\,III}}\right)\right] \end{bmatrix}, \\ \ldots \end{cases} \tag{4}$$

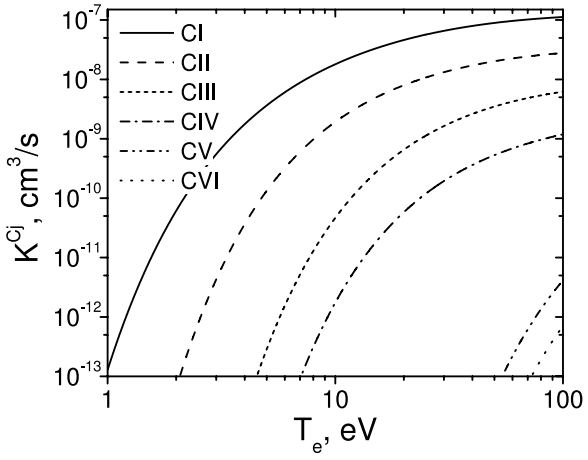

Figure 6. Electron impact ionization rates of carbon species in corona approximation as a function of electron temperature. The curves are plotted using the recommended data from [35].

which gives us the quantity of carbon ion species at a distance $z = u_0 t$ from the particle. Provided the ablation rate is fixed, the total particle current of all carbon species in this solution remains constant at any time and equals I_0. The electron impact ionization rates of the carbon species used here are the rates recommended in [35], and are plotted in figure 6 as a functions of the electron temperature. The relative abundance of the carbon species in the ablated carbon flow calculated according to equation (4) is plotted as a function of time in figure 7(*a*) for $n_e = 10^{13}\,\mathrm{cm}^{-3}$, $T_e = 10\,\mathrm{eV}$ and in figure 7(*b*) for $n_e = 10^{14}\,\mathrm{cm}^{-3}$, $T_e = 30\,\mathrm{eV}$. As can be seen in these figures, we can limit our consideration to carbon species C I–C IV for the characteristic time $\sim 10^{-5}$ s, which corresponds to transit time of a carbon atom/ion through the cloud of size ~ 1 cm with speed $\sim 10^5\,\mathrm{cm\,s}^{-1}$. At the lower plasma densities and temperatures plotted in figure 7(*a*) no significant fraction of carbon ions higher than C III can be produced during the time $\sim 10^{-5}$ s. As follows from these results, the carbon ionization states are far from corona equilibrium during the time interval considered, because for the higher plasma parameters the equilibrium ionization state is almost pure C V that is reached at the time $\sim 10^{-3}$ s and for the lower plasma temperature and density the equilibrium is reached during $\sim 10^{-2}$ s and corresponds to a mix of about equal amounts of C III, C IV and C V ions [36]. The fact that the carbon species in the cloud are far from the equilibrium ionization state also shows that recombination does not play a significant role in the cloud ionization dynamics during the considered time interval and was safely neglected in the model equations equation (3).

6. Radiation of ablation cloud

In order to estimate visibility of the ablation cloud by the camera, we consider line radiation produced due to electron impact excitation of the carbon species C I–C IV, which comprise the majority of the cloud, as was determined in the previous section. In the wavelength range of the camera sensitivity these species have strong lines corresponding to electronic transitions from 2p3p to 2p3s levels. Here we do not resolve the lines corresponding to each sublevel transition and consider envelopes of the lines, which are centred at 908.9 nm for C I, 514.3 nm for C II, 465.0 nm for C III and 580.6 nm for C IV [37]. The considered carbon species have very strong lines corresponding to electron transitions from excited to the ground level $2s^2 2p^2$. However,

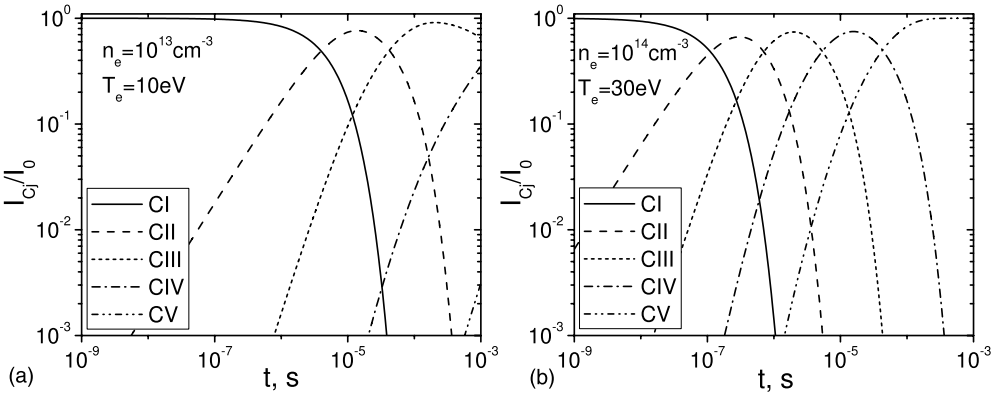

Figure 7. The modelled relative abundance of carbon species in the flow of ablated carbon particles as a function of the time for (*a*) $n_e = 10^{13}$ cm^{-3}, $T_e = 10$ eV and (*b*) $n_e = 10^{14}$ cm^{-3}, $T_e = 30$ eV.

these transitions produce light in UV spectrum [37] that is outside the spectral sensitivity range of the considered camera system.

As the spatial structure of the ablation cloud in magnetic field is complicated, the analysis of which is beyond the scope of this paper, we limit our consideration to line radiation from the central part of the cloud covered by the projected pixel of size $L_{cl} = L_{px}/\beta$ and do not consider other pixels of the cloud image. We assume that radiation from this part of the ablation cloud induces camera signal in the single pixel and neglect line radiation coming to this pixel from outer parts of the cloud. It is also assumed that the surrounding plasma is optically thin for the observed radiation. Then the camera signal (in counts per unit time) induced by the line radiation in the pixel is

$$S_{line} = \frac{n_e}{4\pi L_{cl}^2} \sum_{Cj} \gamma_{Cj}\, \mathcal{PEC}\left(\lambda_{Cj}\right) P\left(\lambda_{Cj}\right), \tag{5}$$

where λ_{Cj} is the wavelength of line radiation from jth carbon specie, $\mathcal{PEC}(\lambda_{Cj})$ is the photon emissivity coefficient corresponding to line λ_{Cj} and $\gamma_{Cj} \equiv \int_0^{L_{cl}/u_0} I_{Cj}(t)\,\mathrm{d}t$ is the number of carbon particles of type j in the considered part of the cloud. Note that the number of particles γ_{Cj} in the cloud is proportional to the dust surface area $4\pi R_d^2$ due to independence of the flux of ablated carbon atoms, Γ_0, from grain size in our model. This leads to the same proportionality of the line radiation signal S_{line} to the factor $\mu^{-1} = \left(L_{px}/\beta R_d\right)^{-2}$, as for the thermal radiation signal in equation (2). Thus, the line radiation signal is also proportional to the square of the dust radius, however, the dependence on distance d is more complex due to changing size of the observed part of the cloud, L_{cl}.

The excitation photon emissivity coefficients $\mathcal{PEC}(\lambda_{Cj})$ used in this paper are obtained from the ADAS database [38] in assumption of collisional–radiative equilibrium of population of the excited levels for each of the considered carbon species. The typical values of the photon emissivity coefficients for the considered lines and plasma parameters are of order of 10^{-9}–10^{-8} cm^3 s^{-1}. We estimate the volumetric power of bremsstrahlung radiation from the ablation cloud within the camera sensitivity wavelength range at $T_e = 30$ eV as $P_{Br} = 10^{-32}(\mathrm{W\,cm^{-3}})n_e \sum_{Cj>CI} Z_{Cj}^2 n_{Cj} \sim 10^{-31}(\mathrm{W\,cm^{-3}})n_e \sum_{Cj>CI} n_{Cj}$, which is much smaller than the volumetric power of the considered line radiation $P_{line} = n_e \sum_{Cj} (hc/\lambda_{Cj})\mathcal{PEC}(\lambda_{Cj})n_{Cj} \sim 10^{-28}(\mathrm{W\,cm^{-3}})n_e \sum_{Cj} n_{Cj}$. Here, Z_{Cj} is the charge number and n_{Cj} is the density of carbon jth charge state. In the same manner it can be

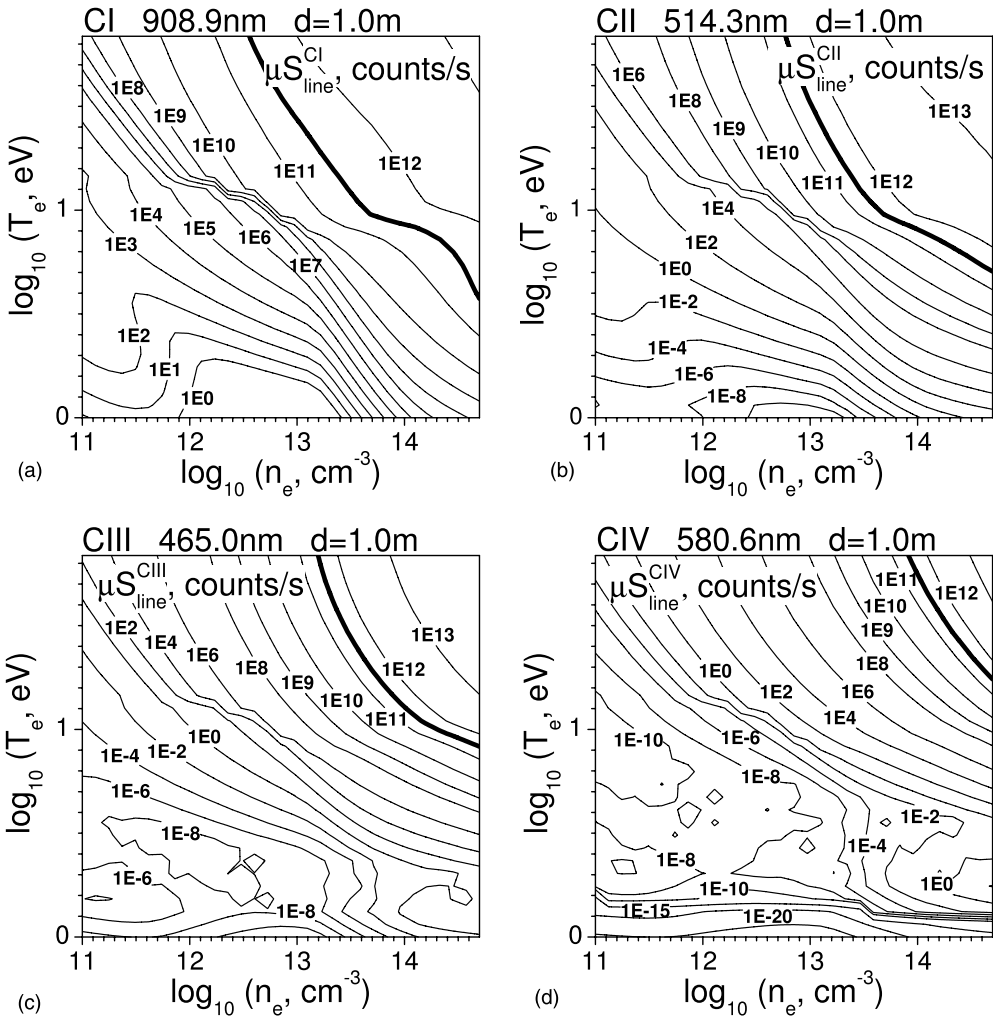

Figure 8. The calculated pixel signal from ablation cloud at distance $d = 1$ m corresponding to the considered lines of (*a*) C I atoms, (*b*) C II, (*c*) C III and (*d*) C IV ions. The thick black curve correspond to the threshold of the radiation visibility by the camera for dust particle of radius $R_d = 1\,\mu$m, assuming 1 ms frame exposure time and 100 counts sensitivity threshold.

shown that the recombination radiation from the ablation cloud is also small in comparison with the line radiation.

In figure 8 the calculated camera signal from the central part of the ablation cloud within the projected pixel at distance $d = 1$ m is plotted as a function of plasma parameters for the C I, C II, C III and C IV lines separately. The thick line corresponds to the threshold visibility of the line radiation produced by the dust particle of radius $R_d = 1\,\mu$m with the camera for 1 ms frame exposure time and 100 counts sensitivity threshold (the same as in figure 5). As can be seen in the figure, the carbon line radiation becomes visible by the camera at much higher plasma densities and temperatures than the dust's thermal radiation shown in figure 5. One can also see in figure 8 that the higher ionization state of the ablated carbon material, the denser and hotter is the surrounding plasma required to see the line radiation.

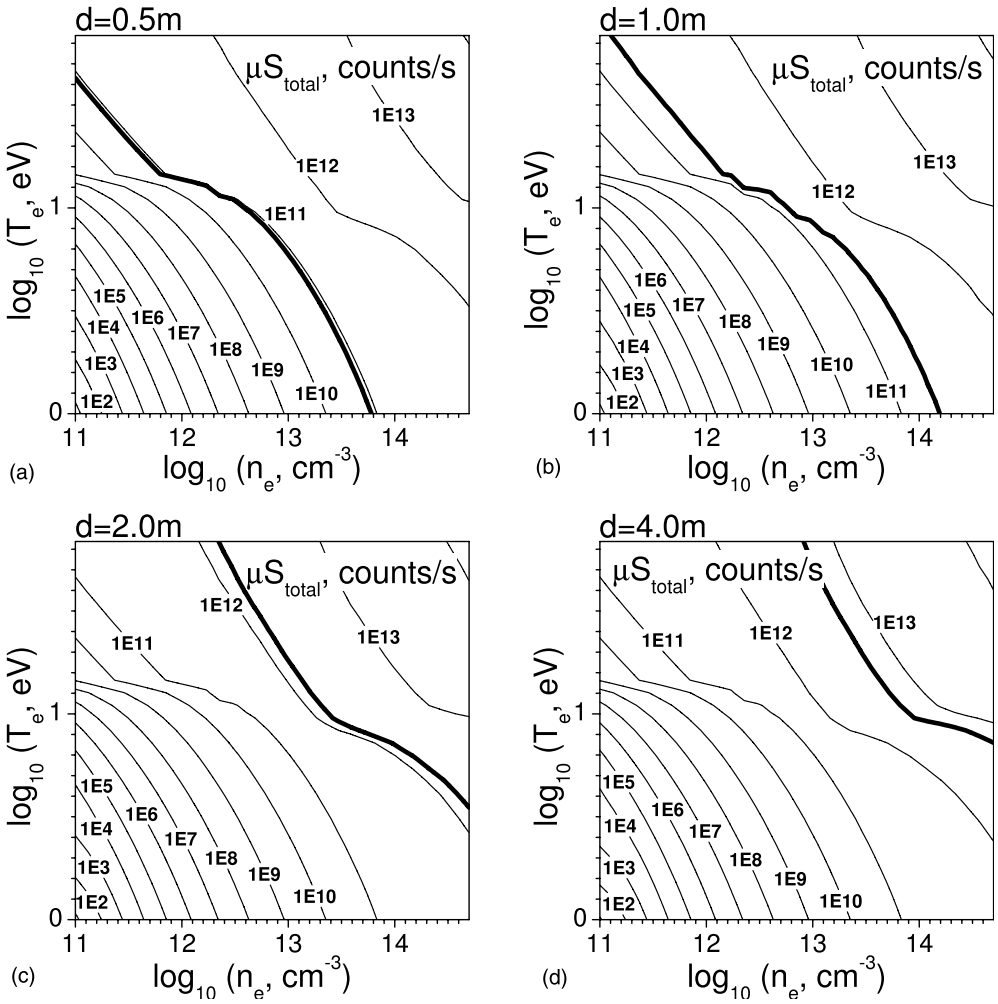

Figure 9. The calculated pixel signal corresponding to total radiation from dust at different distances (*a*) $d = 0.5$ m, (*b*) $d = 1.0$ m, (*c*) $d = 2.0$ m, and (*d*) $d = 4.0$ m. The thick black curve corresponds to the threshold of the radiation visibility by the camera for dust particle of radius $R_d = 1\,\mu$m, assuming 1 ms frame exposure time and 100 counts sensitivity threshold.

7. Dust visibility by camera

Summing the thermal and line radiation from the dust and the ablation cloud calculated in the previous sections, we obtain the total radiation signal $S_{total} = S_{th} + S_{line}$ within the pixel. The dependence of the total signal on plasma parameters is plotted in figure 9 for different distances, d, to the dust particle from the objective lens. The thick curves in the plots indicate the visibility threshold of the radiation from the particle with $R_d = 1\,\mu$m and the same exposure time and threshold sensitivity as in figure 5. As can be seen, the $1\,\mu$m particle placed close to the objective lens just becomes visible in typical SOL plasmas. The dust visibility threshold shifts towards hot and dense plasmas as the distance to the dust increases. Thus, smaller particles in a plasma with fixed parameters become invisible at larger distances due to decrease in the averaged radiance of the dust and the ablation cloud within the increasing projected pixel area.

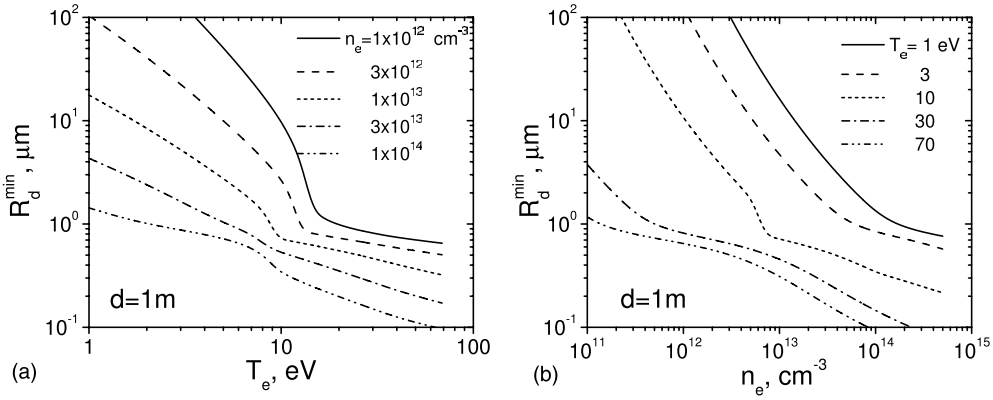

Figure 10. The dependence of minimal size of dust visible with the camera at distance $d = 1$ m on (a) plasma temperature for the various plasma densities and on (b) plasma density for various plasma temperatures assuming 1 ms frame exposure time and 100 counts sensitivity threshold.

In figure 10 the minimal radius of visible dust, R_d^{min}, at distance $d = 1$ m and the same exposure and sensitivity as indicated above is plotted as a function of the plasma temperature and density. One can see that dust of about 1 μm radius or larger is visible in typical SOL plasmas with the camera. For plasma with $n_e = 10^{13}$ cm^{-3} and $T_e = 10$ eV the minimal visible dust radius is $R_d = 0.7$ μm at distance $d = 1$ m, which is in accord with recent DiMES experiments on DIII-D [13, 19]. The smaller sub-micrometre dust may be seen only in very hot and dense plasmas mainly due to line radiation from the cloud. However, we need to keep in mind that small particles in such plasmas can completely ablate in a time shorter than the frame exposure time. In this case, the camera signal will be reduced and the actual minimal size of visible dust would be larger than calculated. Figure 10 also shows that the minimal visible dust size increases sharply as the plasma temperature and density decrease due to decreasing dust temperature and ablation rate in such plasmas. We limit the maximal radius of dust considered here by 100 μm, because the physics of heating and ablation of larger dust may be different from the models used in this paper due to the shielding effects of the high density ablation cloud. Figure 11 shows the dependence of the minimal radius of visible dust on the distance from the dust to the objective lens for various plasma parameters. Due to the proportionality of the camera signal to the factor μ^{-1} the dependence of R_d^{min} on d for all plasma parameters is close to linear, $\sim d$; however, in very hot plasmas, where the contribution of the line radiation from the ablation cloud is large, the dependence becomes slightly weaker.

The relative contributions of the different radiation sources to the total radiation signal in the whole spectral range of the camera are shown in figure 12 as functions of the plasma temperature for $d = 1$ m and $n_e = 10^{13}$ cm^{-3} (a), 3×10^{13} cm^{-3} (b), 10^{14} cm^{-3} (c) and 3×10^{14} cm^{-3} (d). One can see that the thermal radiation signal from the dust grain prevails over the line radiation signal from the ablation cloud in the plasmas with high density 3×10^{14} cm^{-3} and temperatures up to $\sim$8 eV. At the lower plasma densities, the thermal radiation prevails at even higher plasma temperatures up to $\sim$100 eV. In such plasmas the spectral-integrated camera signal may be utilized for measurements of dust temperature or size. As the plasma density and temperature increase the line radiation signal from the ablation cloud starts to dominate. According to the ionization dynamics of the ablation cloud, the line radiation arises subsequently from C I to the higher ionization states as the plasma temperature and density increase. However, because the thermal radiation from the dust particle dominates at the lower

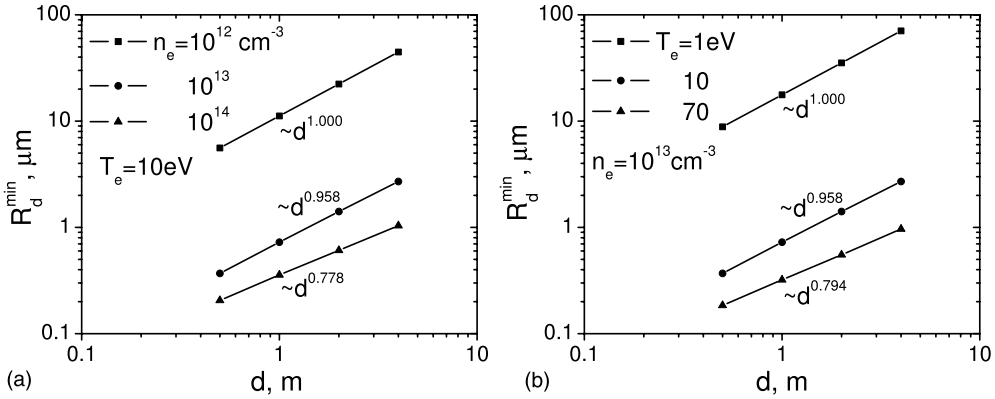

Figure 11. The dependence of minimal size of visible dust on distance d for (a) the various plasma densities at $T_e = 10$ eV and (b) for the various plasma temperatures at $n_e = 10^{13}$ cm^{-3} assuming the same exposure time and the sensitivity threshold as in figure 10.

plasma densities and temperatures, the C I radiation is never the strongest one in the observed cloud volume. Thus, when the cloud radiation signal is stronger than the thermal one, the contribution of the C II and C III lines prevails in the considered plasmas. In figure 13, which shows the relative contributions of the different radiation sources as functions of the distance, d, for $n_e = 10^{14}$cm^{-3} and $T_e = 30$ eV, one can see that the distance to the dust also plays a role in the relative composition of the cloud radiation. As the distance increases, the size of the projected pixel area increases covering larger part of the cloud, which includes larger number of radiating carbon particles, in particular those with higher charge numbers.

In section 3, we mentioned that at high temperatures carbon sublimates mainly in the form of clusters, C_2 and C_3. Thus, the question arises as to whether emission from any C_2 or C_3 in the ablation cloud surrounding the dust grain could contribute significantly to the observed optical emission. The detection of C_3 in carbon plasma radiation appears to be limited to the Swings band which is centred at ~405 nm [39]. Since this is outside of the spectral range of the camera sensitivity discussed in this paper, we can neglect the contribution of this emission. On the other hand, the most prominent band system of C_2 is the Swan band centred at about ~515 nm [40, 41], which does lie within the wavelength range of interest. We can estimate emission in this band using the photon emissivity coefficient for the Swan band given as $\sim 4 \times 10^{-8}$ cm^3 s^{-1} in [42]. (We note that this is only given for electron temperatures from 1 to 6 eV, but appears to flatten out at the higher temperature.) Since this value is comparable to the photon emissivity coefficient for the line radiation of C I, the contribution from Swan band emission would be comparable to that from C I line radiation if the number density of C_2 is comparable to C I. However, we have shown that line radiation from C I is weaker than other kinds of the considered cloud radiation. Therefore, we suggest that the contribution of Swan band radiation to the total radiation would be also small in comparison with the thermal radiation from the dust at the plasma parameters, where clusters do not dissociate quickly. More detailed study of radiation of carbon clusters should be performed in the future.

8. Conclusions

A simple model for carbon dust visibility by modern fast framing cameras was developed, which takes into account both the thermal radiation of the dust grain and line radiation of the

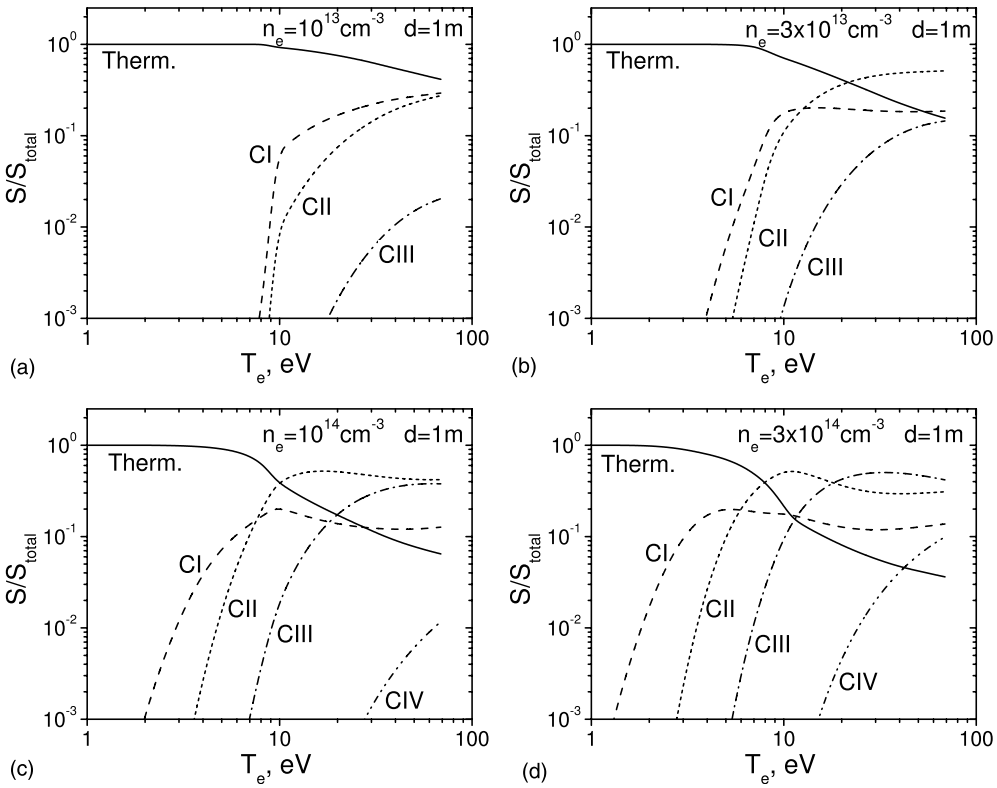

Figure 12. Relative contributions of the different radiation sources in the total radiation signal of dust as functions of the plasma temperature, for $d = 1\,\mathrm{m}$ and (*a*) $n_\mathrm{e} = 10^{13}\,\mathrm{cm}^{-3}$, (*b*) $n_\mathrm{e} = 3 \times 10^{13}\,\mathrm{cm}^{-3}$, (*c*) $n_\mathrm{e} = 10^{14}\,\mathrm{cm}^{-3}$ and (*d*) $n_\mathrm{e} = 3 \times 10^{14}\,\mathrm{cm}^{-3}$.

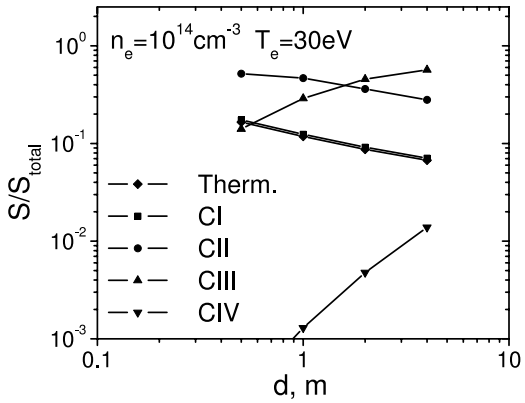

Figure 13. Relative contributions of the different radiation sources in the total dust radiation signal as functions of the distance from the dust to the objective for $n_\mathrm{e} = 10^{14}\,\mathrm{cm}^{-3}$ and $T_\mathrm{e} = 30\,\mathrm{eV}$.

carbon neutrals and ions in the ablation cloud around the grain. The model relates the dust signal recorded by a camera with parameters of dust particles and the surrounding plasma. Applying this model for dust particles in the modelled plasma conditions and the camera system used on DIII-D, the dependences of the minimal size of carbon dust visible with the

test camera on plasma parameters were obtained. It was shown that at parameters typical for SOL plasmas, carbon dust particles of a micrometre size or larger are detectable with the fast framing camera, which is in accord with available experimental data. It was also demonstrated that sub-micrometre dust can be detected with the camera only in hot and dense plasmas, as near the separatrix, the strike points or in the edge localized plasma formations. We also suggest that the dust particles of a sub-micrometre size may be visible in ITER even in far SOL plasmas. However, in divertor regions with dense but relatively cold plasmas the sub-micrometre particles can be still below the visibility threshold. As the plasma temperature and density decrease, the detectable dust size increases sharply. The minimal size of detectable dust is approximately proportional to the distance from the particle to the objective; this implies that smaller particles in the far field camera view may be invisible. The dependence of the minimal detectable dust size on the distance becomes notably weaker than linear proportionality in hot and dense plasmas due to the increasing contribution of the radiation from the ablation cloud.

In the relatively cold plasmas of the far SOL and the divertor regions of present fusion devices the thermal radiation from the carbon dust dominates the line radiation from the cloud. This may allow measurements of dust temperature or size using the spectral-integrated camera signal. The line radiation of the cloud can dominate the thermal radiation of the carbon grain only in the hotter and denser plasmas such as near the separatrix of modern tokamaks or in the SOL of ITER. The low ionization states of carbon, namely, C II and C III, contribute the most to the line radiation from the considered ablation cloud, while the C I radiation is dominated by either line radiation of other carbon species or by the thermal radiation of the grain. The contribution of line radiation from carbon particles of the higher ionization states increases with the plasma temperature, density and the distance from the particle. While a variety of cameras and optical systems can be used in dust measurement experiments on different fusion devices, the dust radiation model developed in this work and the main results obtained may be employed to analyse particular camera data with its specific parameters. In future work we plan to apply the developed model for analysis of 3D dust trajectories recorded in a tokamak discharge with controlled plasma parameters to estimate the size of the visible dust and compare it with dust transport simulation results. The dust radiation model can also be applied for developing a plasma diagnostic technique employing the dust measurements. For instance, measurements of intensity and spectrum of radiation from mobile dust particles with known sizes that the artificially injected into tokamak plasmas may be used to characterize the local plasma density, temperature and flow velocities in different regions of tokamak. Using various dust materials or dust consisting of different materials may help to get a desirable blend of thermal radiation from the dust and the line radiation from the ablation cloud extending applicability of the method. Further analysis of structure and dynamics of the ablation cloud in magnetic fields may be useful for studies of impurity transport in fusion devices.

Acknowledgments

This work was partially supported by the US DoE under grant DE-FG02-04ER54852. We also like to thank to our colleagues and collaborators D L Rudakov, W P West, A Kreter, A Litnovsky, D Nishijima and D A Mendis for useful discussions.

References

[1] Sharpe J P, Petti D A and Bartels H-W 2002 *Fusion Eng. Des.* **63–64** 153
[2] Winter J 2004 *Plasma Phys. Control. Fusion* **46** B583

[3] Girard J-Ph, Garin P, Taylor N, Uzan-Elbez J, Rodriguez-Rodrigo L and Gulden W 2007 *Fusion Eng. Des.* **82** 506
[4] Krasheninnikov S I, Tomita Y, Smirnov R D and Janev R K 2004 *Phys. Plasmas* **11** 3141
[5] Krasheninnikov S I, Smirnov R D, Benson D J, Pigarov A Yu, Soboleva T K, Rognlien T D, Rosenberg M, Shevchenko V I, Shukla P K and Mendis D A 2006 *Proc. 21st IAEA Fusion Energy Conference (Chengdu, China)* IAEA-CN-149/TH/P6-18
[6] Saito K *et al* 2007 *J. Nucl. Mater.* **363–365** 1323
[7] Pigarov A Yu, Krasheninnikov S I, Soboleva T K and Rognlien T D 2005 *Phys. Plasmas* **12** 122508
[8] Smirnov R D, Pigarov A Yu, Rosenberg M, Krasheninnikov S I and Mendis D A 2007 *Plasma Phys. Control. Fusion* **49** 347
[9] Martin J D, Bacharis M, Coppins M, Counsell G F and Allen J E 2008 *Euro. Phys. Lett.* **83** 65001
[10] Roquemore A L, Nishino N, Skinner C H, Bush C, Kaita R, Maqueda R, Davis W, Pigarov A Yu and Krasheninnikov S I 2007 *J. Nucl. Mater.* **363–365** 222
[11] West W P, Bray B D and Burkart J 2006 *Plasma Phys. Control. Fusion* **48** 1661
[12] West W P and Bray B D 2007 *J. Nucl. Mater.* **363–365** 107
[13] Rudakov D L *et al* 2007 *J. Nucl. Mater.* **363–365** 227
[14] Voinier C, Skinner C H and Roquemore A L 2005 *J. Nucl. Mater.* **346** 266
[15] Parker C V, Skinner C H and Roquemore A L 2007 *J. Nucl. Mater.* **363–365** 1461
[16] Counsell G, de Vere A P C, Braithwaite N St J, Hiller S and Bjorkman P 2006 *Rev. Sci. Instrum.* **77** 093501
[17] Skinner C H, Roquemore A L, the NSTX team, Bader A and Wampler W R 2004 *Rev. Sci. Instrum.* **75** 4213
[18] Lasnier C J *et al* 2008 *Fusion Sci. Technol.* **53** 640
[19] Yu J H, Rudakov D L, Pigarov A Yu, Smirnov R D, Brooks N H, Muller S H and West W P 2009 Fast camera imaging of dust in the DIII-D tokamak *J. Nucl. Mater.* at press doi:10.1016/j.jnucmat.2009.01.053
[20] Bader A, Granetz R, LaBombard B and Terry J 2008 Diagnostics to study flow of dust particles in scrape-off layer of Alcator C-Mod plasmas *Bull. Am. Phys. Soc.* **52** (16) 216
[21] Ratynskaia S, Castaldo C, Giovannozzi E, Rudakov D, Morfill G, Horanyi M, Yu J H and Maddaluno G 2008 *Plasma Phys. Control. Fusion* **50** 124046
[22] Rudakov D L *et al* 2008 *Rev. Sci. Instrum.* **79** 10F303
[23] Parks P B and Turnbull R I 1978 *Phys. Fluids* **21** 1735
[24] Krasheninnikov S I *et al* 2008 *Plasma Phys. Control. Fusion* **50** 124054
[25] Yu J H and Van Zeeland M A 2008 *Rev. Sci. Instrum.* **79** 10F516
[26] http://www.visionresearch.com
[27] Landau L D and Lifshitz E M 1958 *Course of Theoretical Physics vol 5: Statistical Physics* (London: Pergamon) pp 256–7
[28] Haines J R and Tsai C C *Graphite Sublimation Tests for the Muon Collider/Neutrino Factory Target Development Program* (report ORNL/TM-2002/27) http://www.ornl.gov/∼webworks/cppr/y2002/rpt/113138.pdf
[29] Chase M W Jr (ed) 1998 NIST-JANAF Thermochemical Tables I *J. Phys. Chem. Ref. Data (Monograph vol 9)* (Washington, DC and New York: AIP and ACS for NIST) pp 550, 551, 661, 686, 691, 696
[30] Bohren C F and Huffman D R 1983 *Absorption and Scattering of Light by Small Particles* (New York: Wiley)
[31] Rosenberg M, Smirnov R D and Pigarov A Yu 2008 *J. Phys. D: Appl. Phys.* **41** 015202
[32] Mie G 1908 *Ann. Phys., Lpz. (Library translation 1873, Royal Aircraft Establishment)* **25** 377
[33] Smirnov R D, Krasheninnikov S I, Pigarov A Yu, Beson D J, Rosenberg M and Mendis D A 2009 Modeling of velocity distributions of dust in tokamak edge plasmas and dust–wall collisions *J. Nucl. Mater.* at press doi:10.1016./j.jnucmat.2009.01.090
[34] Schultz D R and Krstić P S 2002 *Phys. Plasmas* **9** 64
[35] Lennon M A, Bell K L, Gilbody H B, Hughes J G, Kingston A E, Murray M J and Smith F J 1988 *J. Phys. Chem. Ref. Data* **17** 1285
[36] Carolan P G and Piotrowicz V A 1983 *Plasma Phys.* **25** 1065
[37] Ralchenko Yu, Kramida A E, Reader J and NIST ASD Team 2008 *NIST Atomic Spectra Database* (version 3.1.5) (Gaithersburg, MD: National Institute of Standards and Technology) http://physics.nist.gov/asd3
[38] Summers H P 2004 *The ADAS User Manual* (version 2.6) http://adas.phys.strath.ac.uk
[39] Nemes L, Keszler A M, Parigger C G, Hornkohl J O, Michelsen H A and Stakhursky V 2007 *Appl. Opt.* **46** 4032
[40] Van Orden A and Saykally R 1998 *Chem. Rev.* **98** 2313
[41] Sasaki K, Wakasaki T and Kadota K 2002 *Appl. Surf. Sci.* **197–198** 197
[42] Fantz U, Meir S and ASDEX Upgrade Team 2005 *J. Nucl. Mater.* **337–339** 1087